Engineering Structures 33 (2011) 1479–1490

Contents lists available at ScienceDirect

Engineering Structures

journal homepage: www.elsevier.com/locate/engstruct

Nonlinear finite element analysis of CFT-to-bracing connections subjected to axial compressive forces

Hsuan-Teh Hu [a,*], Chun-Wei Chen [b], Mei-Yun Huang [b]

[a] Department of Civil Engineering and Sustainable Environment Research Center, National Cheng Kung University, Tainan, Taiwan, ROC
[b] Department of Civil Engineering, National Cheng Kung University, Tainan, Taiwan, ROC

ARTICLE INFO

Article history:
Received 17 January 2009
Received in revised form
27 January 2010
Accepted 21 January 2011
Available online 26 February 2011

Keywords:
Concrete-filled tube
Bracing
Axial force
Finite element analysis

ABSTRACT

The Abaqus finite element program together with nonlinear material constitutive models for concrete-filled tube (CFT) and steel gusset plate is used to analyze the behaviors of the gusset plate type CFT-to-Bracing connections subjected to axial compressive forces. It is found that the failure of CFT-to-Bracing connections occurs below the connecting area. Local bulged shapes of the steel tube might take place in the areas close to the gusset plate and the fixed end under the failure stage. The ultimate strengths of the CFT columns slightly increase with the increasing of the load ratio and the thickness of the gusset plate. The introduction of the cutouts on the gusset plates slightly increases the ultimate strength of the CFT column and causes more local bulged shapes on the steel tubes below the connection area under the failure stage.

1. Introduction

A concrete-filled tube (CFT) column consists of a steel tube filled with concrete. Due to the benefit of composite action of both materials, the CFT columns provide excellent seismic resistant structural properties such as high strength, high ductility and large energy absorption capacity. Therefore, CFT columns have gained popularity in supporting heavy loads in high-rise buildings, bridges and offshore structures. Various experimental and analytical studies have been performed on CFT columns [1–17] and special interests have been focused on the connection regions [18–24].

The aim of this investigation is to employ the nonlinear finite element program Abaqus [25] to perform numerical simulations of the gusset plate type CFT-to-bracing connections (Fig. 1) subjected to axial compressive forces P_a and P_g. To achieve this goal, proper material constitutive models for steel gusset plate, steel tube and concrete core are proposed. Then the proposed material constitutive models are verified against experimental data of Yang [26]. Finally, the influence of the thickness of the gusset plate, the cutouts on the gusset plate and the type of loading on the behavior of CFT-to-Bracing connections are studied and discussed.

2. Material properties and constitutive models

The experiment for CFT-to-bracing connections subjected to axial compressive forces (Fig. 1) was carried out by Yang [26]. There are seventeen specimens in total (Table 1). These CFT columns are subjected to compressive forces P_a and P_g to the end of the columns and the gusset plates, respectively. The tested specimens can be categorized into three groups. The first group of the CFT column contains the S specimen which has no gusset plate at all. The S specimen is subjected to axial compressive force P_a to the end only. The second group of the CFT columns contains the P specimens. The first number after P is the thickness of the gusset plate (in mm), which could be 12, 24 and 36. The second number after P is the load ratio $P_a/(P_a + P_g)$ in terms of percentage. For example, P24-67 specimen stands for CFT column having a gusset plate with 24 mm thickness and a load ratio $P_a/(P_a + P_g) = 67\%$. The third group of the CFT columns contains the PH specimens. Same as the P specimens, the first number after PH is the thickness of the gusset plate and the second number after PH is the load ratio. However, the gusset plates of the PH specimens contain circular cutouts. The 24 mm gusset plate has 2 circular holes and the 36 mm gusset plate has 3 circular holes. The dimensions and positions of these holes on the gusset plates are shown in Fig. 2. From Table 1, we can observe that the length H of the S specimen is equal to 795 mm. The length of the rest P and PH specimens is equal to 1590 mm. The diameter D and the thickness t of all the tubes are equal to 265 mm and 7 mm, respectively.

* Corresponding author. Tel.: +886 6 2757575x63168; fax: +886 6 2358542.
E-mail address: hthu@mail.ncku.edu.tw (H.-T. Hu).

0141-0296/$ – see front matter © 2011 Elsevier Ltd. All rights reserved.
doi:10.1016/j.engstruct.2011.01.018

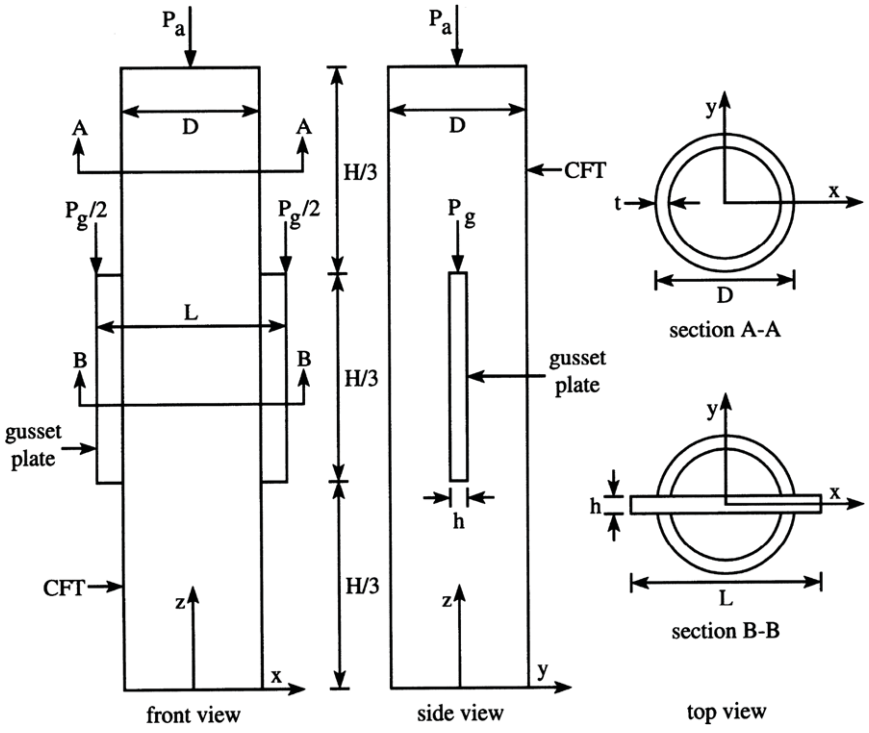

Fig. 1. Geometry and loading of gusset plate type CFT-to-Bracing connection.

Table 1
Dimensions and load ratios of CFT columns.

Specimen	H (mm)	D (mm)	L (mm)	t (mm)	h (mm)	D/t	Numbers of holes on gusset plate	Load ratio $P_a/(P_a+P_g)$ (%)
S	795	265	320	7	–	37.86	0	100
P12-00	1590	265	320	7	12	37.86	0	0
P12-33	1590	265	320	7	12	37.86	0	33
P12-67	1590	265	320	7	12	37.86	0	67
P24-00	1590	265	320	7	24	37.86	0	0
P24-33	1590	265	320	7	24	37.86	0	33
P24-67	1590	265	320	7	24	37.86	0	67
P24-100	1590	265	320	7	24	37.86	0	100
P36-00	1590	265	320	7	36	37.86	0	0
P36-33	1590	265	320	7	36	37.86	0	33
P36-67	1590	265	320	7	36	37.86	0	67
PH24-00	1590	265	320	7	24	37.86	2	0
PH24-33	1590	265	320	7	24	37.86	2	33
PH24-67	1590	265	320	7	24	37.86	2	67
PH36-00	1590	265	320	7	36	37.86	3	0
PH36-33	1590	265	320	7	36	37.86	3	33
PH36-67	1590	265	320	7	36	37.86	3	67

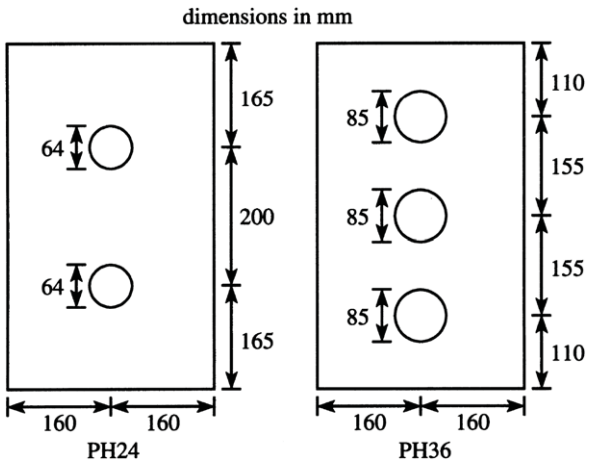

Fig. 2. Cutouts on the gusset plates.

2.1. Steel tube and steel gusset plate

In the analysis, Poisson's ratio ν_s and the elastic modulus E_s of the steel tube and steel gusset plate are assumed to be 0.3 and 200 GPa, respectively. The uniaxial behavior of the steel tube and the steel gusset plate is modeled by a piecewise linear model and their stress–strain curves used in the analysis are shown in Fig. 3.

When the steel tube and the steel gusset plate are subjected to multiple stresses, a von Mises yield criterion is employed to define the initial yield surface, which is written as

$$F = \sqrt{3J_2} - \sigma_y = \frac{1}{\sqrt{2}}\sqrt{(\sigma_1-\sigma_2)^2+(\sigma_2-\sigma_3)^2+(\sigma_3-\sigma_1)^2} - \sigma_y = 0 \quad (1)$$

where J_2 is the second stress invariant of the stress deviator tensor and σ_1, σ_2, and σ_3 are the principal stresses. Fig. 4 shows the von Mises yield surface in the three-dimensional principal stress space. The response of the steel tube and the steel gusset plate

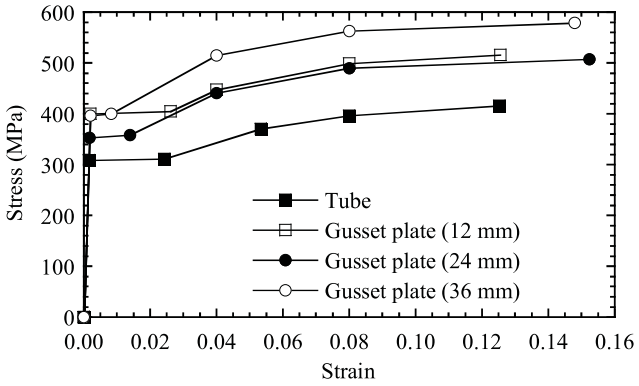

Fig. 3. Stress–strain curves of steel tube and steel gusset plate.

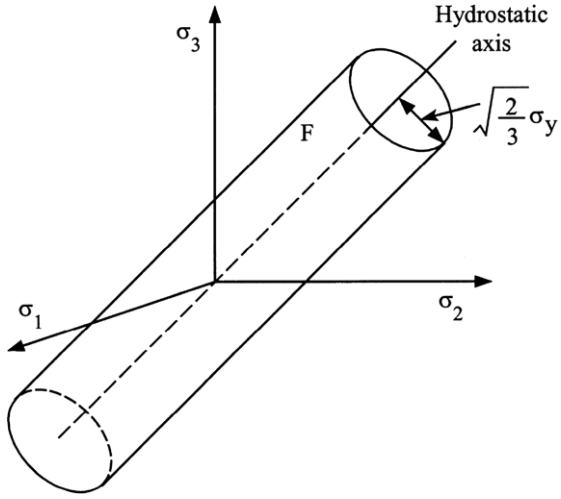

Fig. 4. Von Mises yield surface in the three-dimensional principal stress space.

is modeled by an elastic hardening plastic theory with isotropic hardening rule and associated flow rule. When plastic deformation occurs, there should be a certain parameter to guide the expansion of the yield surface. A commonly used approach is to relate the multidimensional stress and strain conditions to a pair of quantities, namely, the effective stress f_s and effective strain ε_s, such that results obtained following different loading paths can all be correlated by means of the equivalent uniaxial stress–strain curve. In this investigation, the uniaxial stress–strain curves given in Fig. 3 are used as the equivalent uniaxial stress–strain curve for the steel tube and the steel gusset plate. As the result, the subsequent yield surfaces of the tube and the gusset plate can be written as

$$F = \sqrt{3J_2} - f_s = \frac{1}{\sqrt{2}}\sqrt{(\sigma_1-\sigma_2)^2+(\sigma_2-\sigma_3)^2+(\sigma_3-\sigma_1)^2} - f_s = 0. \quad (2)$$

2.2. Concrete

Poisson's ratio ν_c of concrete under uniaxial compressive stress ranges from 0.15 to 0.22, with a representative value of 0.19 or 0.20 [27]. In this study, Poisson's ratio of concrete is assumed to be 0.2.

Let the uniaxial compressive strength and the corresponding strain of the unconfined concrete be f_c' and ε_c' (Fig. 5). The value of ε_c' is usually around the range of 0.002–0.003. A representative value 0.002 is used in the analysis. When concrete is subjected to

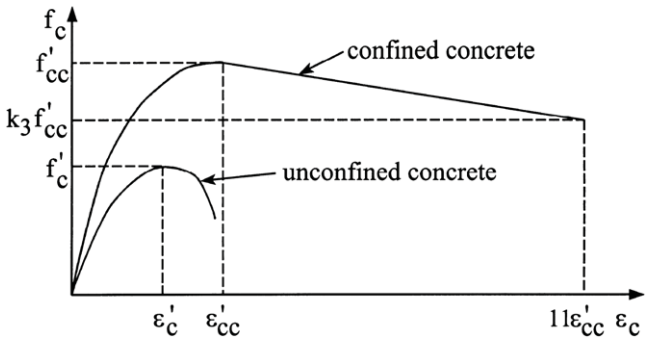

Fig. 5. Equivalent uniaxial stress–strain curve for concrete.

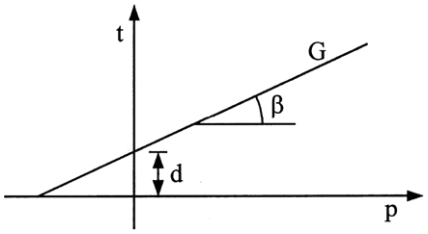

Fig. 6. Linear Drucker–Prager yield criterion for concrete.

laterally confining pressure, the uniaxial compressive strength f_{cc}' and the corresponding strain ε_{cc}' (Fig. 5) are much higher than those of unconfined concrete. The relations between f_{cc}', f_c' and between ε_{cc}', ε_c' are estimated by the following equations [28]:

$$f_{cc}' = k_4 f_c' + k_1 f_l \quad (3)$$

$$\varepsilon_{cc}' = \varepsilon_c'\left(1 + k_2\frac{f_l}{f_c'}\right) \quad (4)$$

where f_l represents the confining pressure around the concrete core. The coefficients k_1 and k_2 are constants and can be obtained from experimental data. Though, Eqs. (3) and (4) are proposed by Mander et al. [28], they have been adopted by many researchers [29–36]. Meanwhile, the coefficients k_1 and k_2 are set to 4.1 and 20.5 based on the studies of Richart et al. [37]. The original form of Eq. (3) was proposed for concrete subjected to hydrostatic pressure [28] and did not contain the strength factor k_4. For CFT subjected to bending moment, part of the concrete may be subject to tensile stress, which is different from the hydrostatic pressure condition. Therefore, a strength factor k_4 is introduced by the authors [15] with the limitation $0 \le k_4 \le 1$.

The concrete in the CFT columns is subjected to triaxial compressive stresses and the failure of concrete is dominated by a compressive failure surface expanding with the increasing of hydrostatic pressure. Hence, a linear Drucker–Prager yield criterion G (Fig. 6) is used to model the yield surface of concrete, which is expressed as

$$G = t - p\tan\beta - d = 0 \quad (5)$$

where

$$p = -(\sigma_1+\sigma_2+\sigma_3)/3 \quad (6a)$$

$$d = \left(1 - \frac{\tan\beta}{3}\right) f_{cc}' \quad (6b)$$

$$t = \frac{\sqrt{3J_2}}{2}\left[1 + \frac{1}{K} - \left(1-\frac{1}{K}\right)\left(\frac{r}{\sqrt{3J_2}}\right)^3\right] \quad (6c)$$

$$r = \left[\frac{9}{2}(S_1^3+S_2^3+S_3^3)\right]^{1/3} \quad (6d)$$

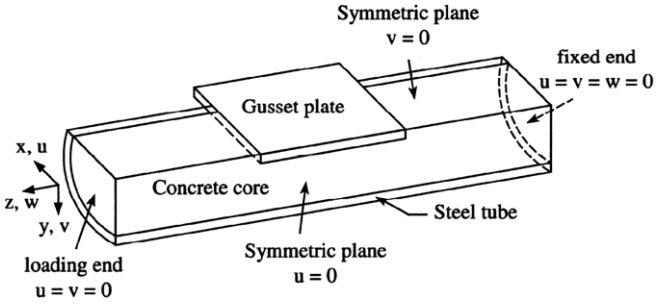

Fig. 7. Conceptual sketch and finite element modeling of CFT-to-bracing connection.

and S_1, S_2, and S_3 are principal stress deviators. The constants K and β are material parameters determined from experimental data. In the analysis, K and β are set to 0.8 and 20°, respectively [14,15].

The response of the concrete is also modeled by an elastic hardening plastic theory with isotropic hardening rule and associated flow rule. The stress–strain relationship proposed by Saenz [38] has been widely adopted as the uniaxial stress–strain curve for concrete and it has the following form:

$$f_c = \frac{E_c \varepsilon_c}{1 + (R + R_E - 2)\left(\frac{\varepsilon_c}{\varepsilon'_{cc}}\right) - (2R - 1)\left(\frac{\varepsilon_c}{\varepsilon'_{cc}}\right)^2 + R\left(\frac{\varepsilon_c}{\varepsilon'_{cc}}\right)^3} \tag{7}$$

where

$$R = \frac{R_E(R_\sigma - 1)}{(R_\varepsilon - 1)^2} - \frac{1}{R_\varepsilon}, \quad R_E = \frac{E_c \varepsilon'_{cc}}{f'_{cc}}$$

and $R_\sigma = 4$, $R_\varepsilon = 4$ may be used [39]. The initial modulus of elasticity of concrete E_c is highly correlated to its compressive strength and can be calculated with reasonable accuracy from the empirical equation [40]:

$$E_c = 4700\sqrt{f'_{cc}}\ \text{MPa}. \tag{8}$$

In the analysis, Eq. (7) is taken as the equivalent uniaxial stress–strain curve for concrete when the concrete strain ε_c is less than ε'_{cc} (Fig. 4). When $\varepsilon_c > \varepsilon'_{cc}$, a linear descending line is used to model the softening behavior of concrete. If k_3 is defined as the material degradation parameter, the descending line is assumed to be terminated at the point where $f_c = k_3 f'_{cc}$ and $\varepsilon_c = 11\varepsilon'_{cc}$ [14,15].

3. Finite element model for CFT columns

The specimens for CFT-to-bracing connections subjected to axial compression force have been shown in Fig. 1. Due to symmetry, only one fourth of the CFT-to-bracing connection is analyzed (Fig. 7). Symmetric boundary conditions are enforced on the symmetric planes, which are $u = 0$ on the front surface of the element mesh and $v = 0$ on the top surface of the element mesh surface. To model the fixed end condition, $u = v = w = 0$ are set at the right surface of the element mesh. In addition, $u = v = 0$ are set at the left surface of the element mesh to simulate the boundary condition of the loading end.

In the finite element mesh, the concrete core, the steel tube and the steel gusset plate are all modeled by 8-node isoparametric solid elements (three degrees of freedom per node) with reduced integration rule. There are three interfaces existed in the finite element mesh, which are the concrete–tube interface, the concrete–gusset plate interface and the tube–gusset plate interface. All these interfaces are modeled by pairs of contact surfaces. The nodes on these interfaces are connected through the contact surfaces that require matching meshes on the both sides of the interfaces. These contact surfaces can model infinitesimal

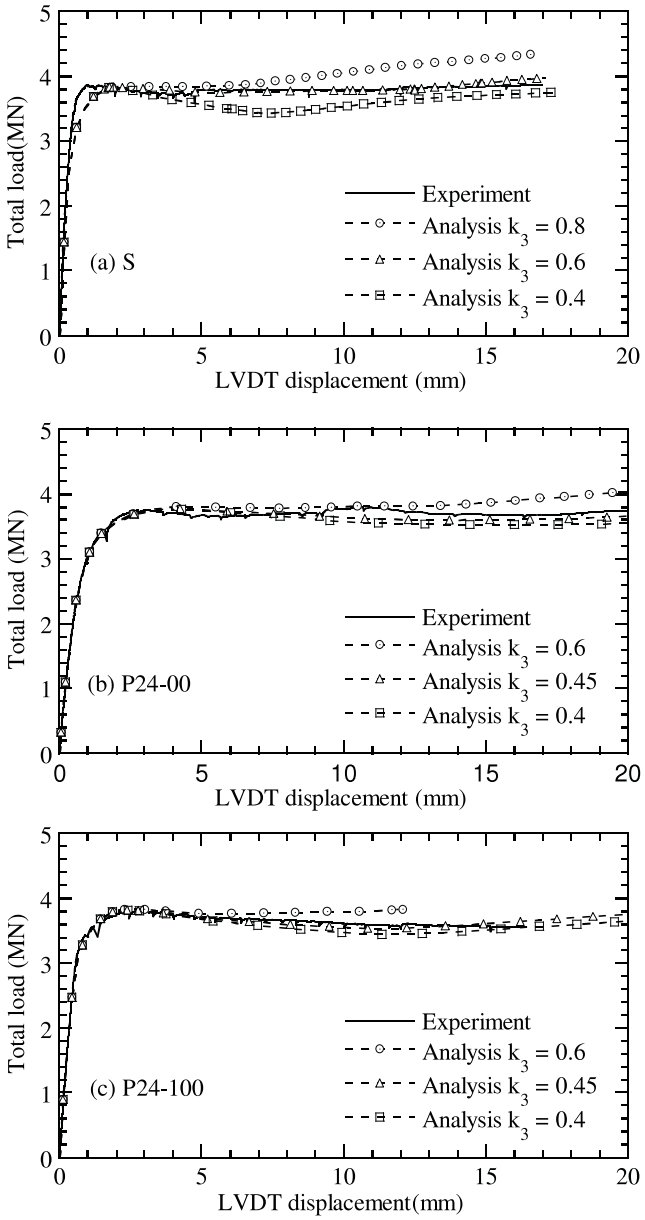

Fig. 8. Simulation of k_3 for specimens S, P24-00 and P24-100 ($k_4 = 0.75$).

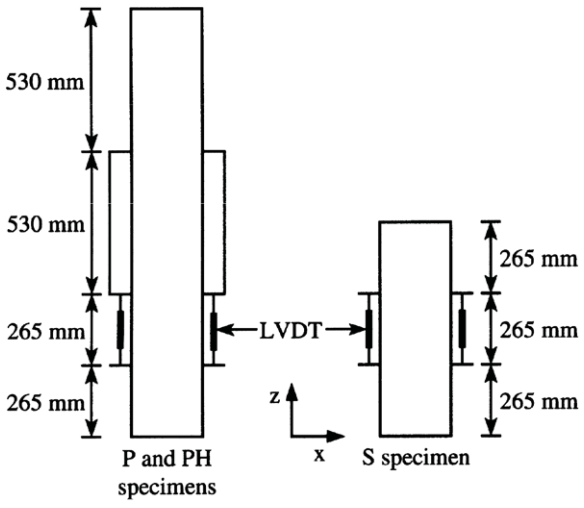

Fig. 9. Positions of LVDT for CFT specimens.

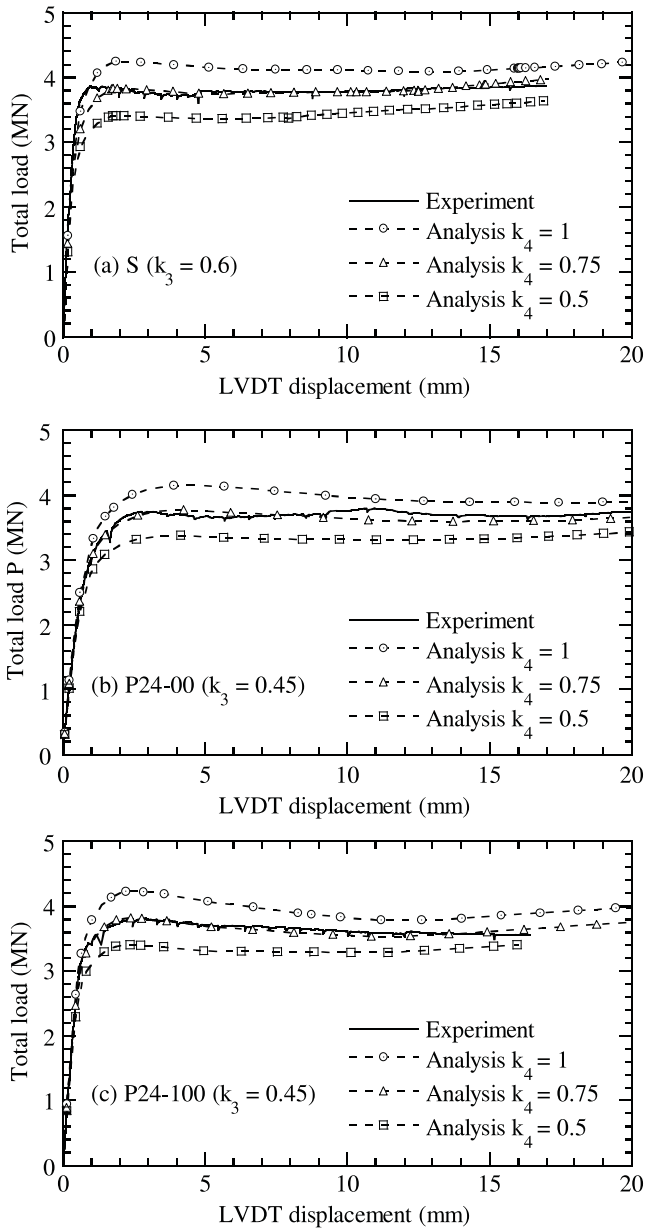

Fig. 10. Simulation of k_4 for specimens S, P24-00 and P24-100.

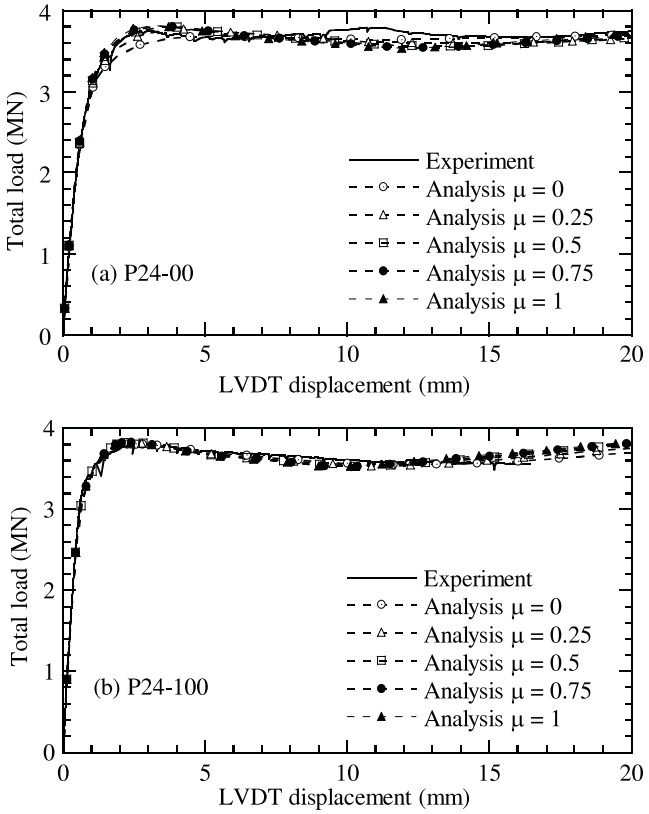

Fig. 11. Influence of the friction coefficient on the behavior of CFT columns.

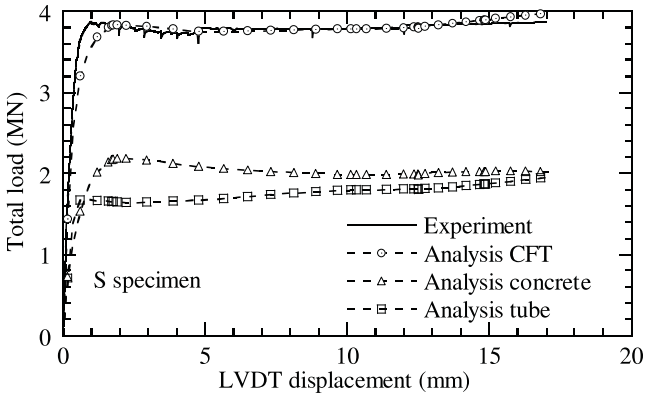

Fig. 12. Load–displacement curves of specimen S.

Table 2
Results of numerical simulations.

Specimen	Ultimate Load (MN)		Error (%)	f_l (MPa)	k_3	k_4
	Experiment	Analysis				
S	3.876	3.834	1.08	3.748	0.45	0.75
P12-00	3.693	3.775	2.22	3.748	0.6	0.75
P12-33	3.897	3.743	3.95	3.748	0.6	0.75
P12-67	3.871	3.805	1.70	3.748	0.6	0.75
P24-00	3.755	3.773	0.48	3.748	0.6	0.75
P24-33	3.862	3.796	1.71	3.748	0.6	0.75
P24-67	3.921	3.803	3.01	3.748	0.6	0.75
P24-100	3.803	3.812	0.24	3.748	0.6	0.75
P36-00	3.865	3.770	2.46	3.748	0.6	0.75
P36-33	4.154	3.794	8.67	3.748	0.6	0.75
P36-67	4.014	3.806	5.18	3.748	0.6	0.75
PH24-00	3.847	3.782	1.69	3.748	0.6	0.75
PH24-33	3.920	3.803	2.98	3.748	0.6	0.75
PH24-67	4.041	3.810	5.72	3.748	0.6	0.75
PH36-00	3.742	3.802	1.60	3.748	0.6	0.75
PH36-33	4.052	3.811	6.32	3.748	0.6	0.75
PH36-67	4.051	3.814	5.85	3.748	0.6	0.75

sliding and friction [25]. The friction coefficient used in all the analyses is $\mu = 0.25$ [14,15]. As the results, the nodes on the interfaces are allowed to either contact or separate but not to penetrate each other.

Convergent studies of the finite element meshes have been done by the authors using various element sizes for CFT columns [41]. It has been shown that the numerical results are not too sensitive to the element sizes and mesh refinements. All the finite element meshes used in the analysis can be seen in the deformation plots of the following section.

4. Numerical analysis

In order to carry out the numerical analysis, the parameters f_l, k_3 and k_4 of the confined concrete should be provided to completely define the equivalent uniaxial stress–strain relation. Based on the suggestion by previous research [14], the following empirical

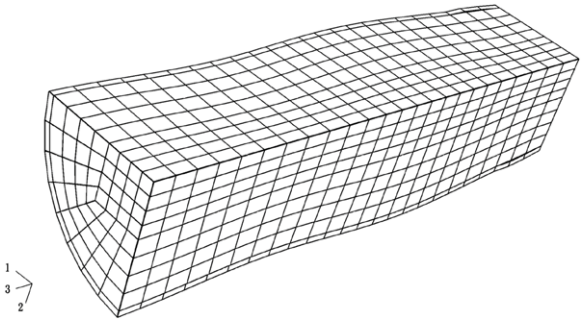

Fig. 13. Deformation shape of specimen S.

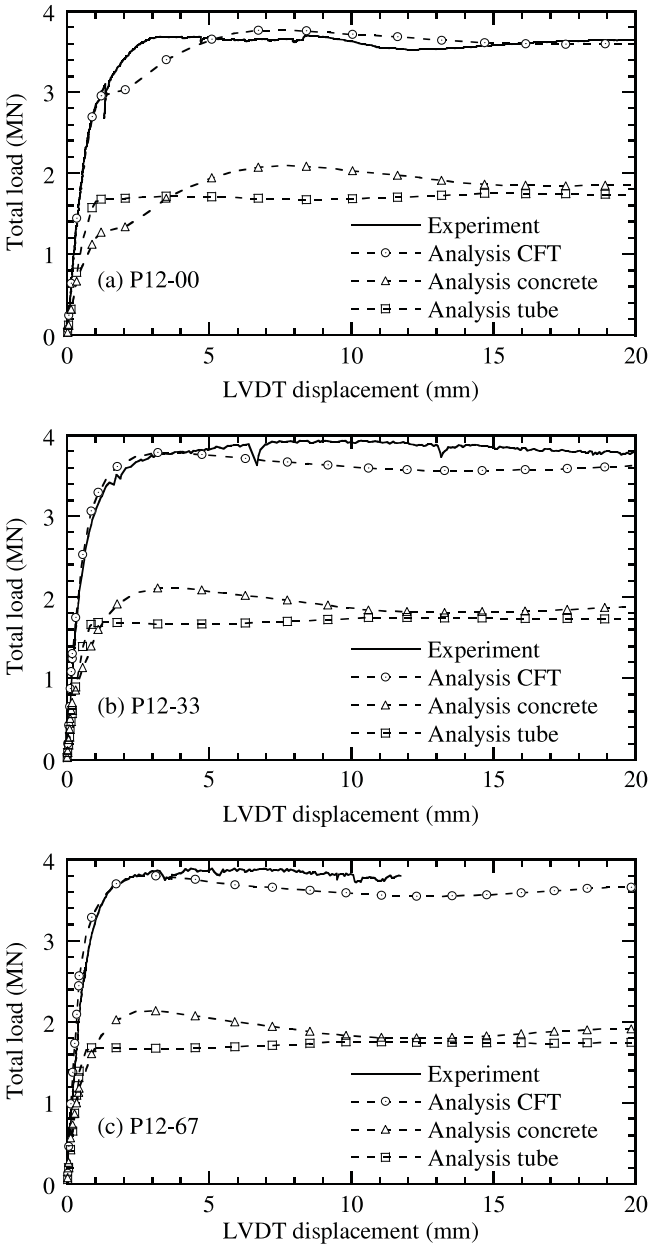

Fig. 14. Load–displacement curves of specimens P12-00, P12-33 and P12-67.

expression is used to calculate the lateral confining pressure of concrete f_l.

$$f_l/f_y = 0.043646 - 0.000832(D/t) \quad (21.7 \le D/t \le 47) \tag{9}$$

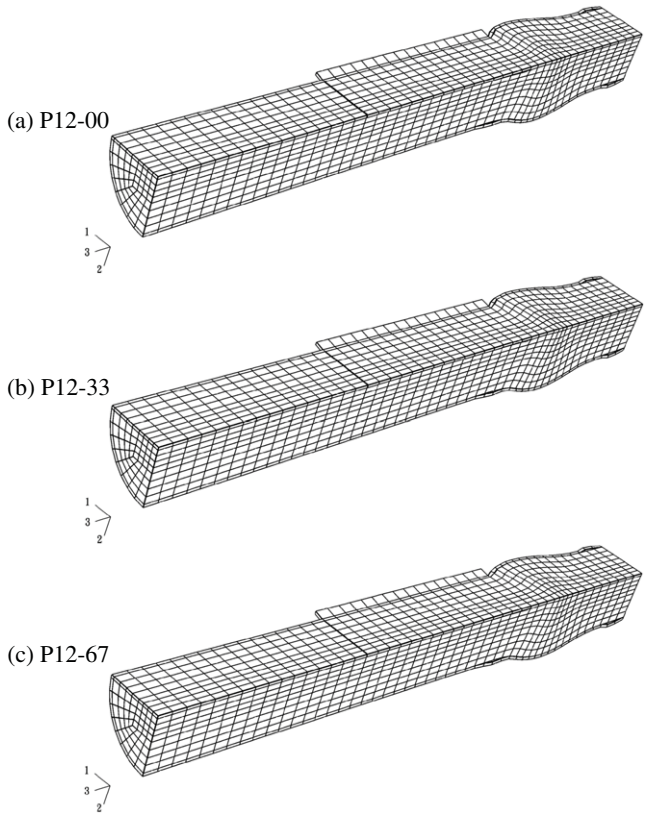

Fig. 15. Deformation shapes of specimens P12-00, P12-33 and P12-67.

where $f_y = 308.5$ MPa is the yield stress of the steel tube. Since the D/t value of all the specimens is equal to 37.86, we obtain $f_l = 3.748$ MPa and this value is used in all the analyses.

The values of the parameters k_3 and k_4 apparently depend on the cross-sectional geometry and material properties. Consequently, their appropriate values are determined by matching the numerical results with experimental data via parametric studies in the following sections.

4.1. Simulation of the material degradation parameter k_3

To make a proper selection of the material degradation parameter k_3, different values of k_3 are simulated for CFT specimens S, P24-00 and P24-100. The selected values of k_3 are $k_3 = 0.4$ 0.45, 0.6 and 0.8, respectively. Based on $k_4 = 0.75$, the load–displacement curves of the experimental data and the numerical results for those specimens are shown in Fig. 8. The vertical axes and the horizontal axes of the figure are the total load $P = P_a + P_g$ and the shortening of the LVDT displacement transducer. The positions of the LVDT displacement transducers on the CFT columns in the experimental set up are shown in Fig. 9. From Fig. 8(a), we can observe that the numerical result with $k_3 = 0.6$ are in good agreement with the experimental data of specimen S. From Fig. 8(b) and (c), we can observe that the numerical results with $k_3 = 0.45$ are in good agreement with the experimental data of specimens P24-00 and P24-100. The reason that the value of k_3 for specimen S is greater than those for specimens P24-00 and P24-100 is because the S specimen does not have a gusset plate. Since there are no cutouts on the tube, specimen S would have a better confining effect than specimens P24-00 and P24-100. As the result, after the ultimate strength of the concrete has been reached, the concrete strength of the CFT column without gusset plate is stronger than those with gusset plate. Similar results are also observed for other CFT columns. Therefore, in the following

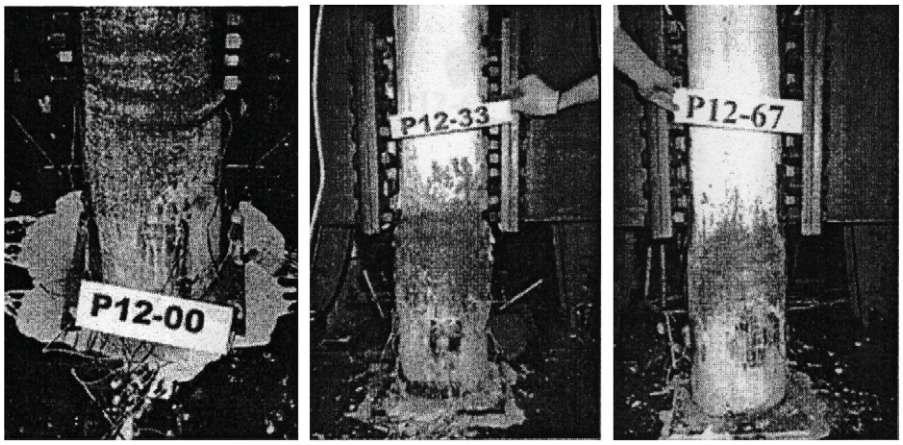

Fig. 16. Failure patterns of specimens P12-00, P12-33 and P12-67 [26].

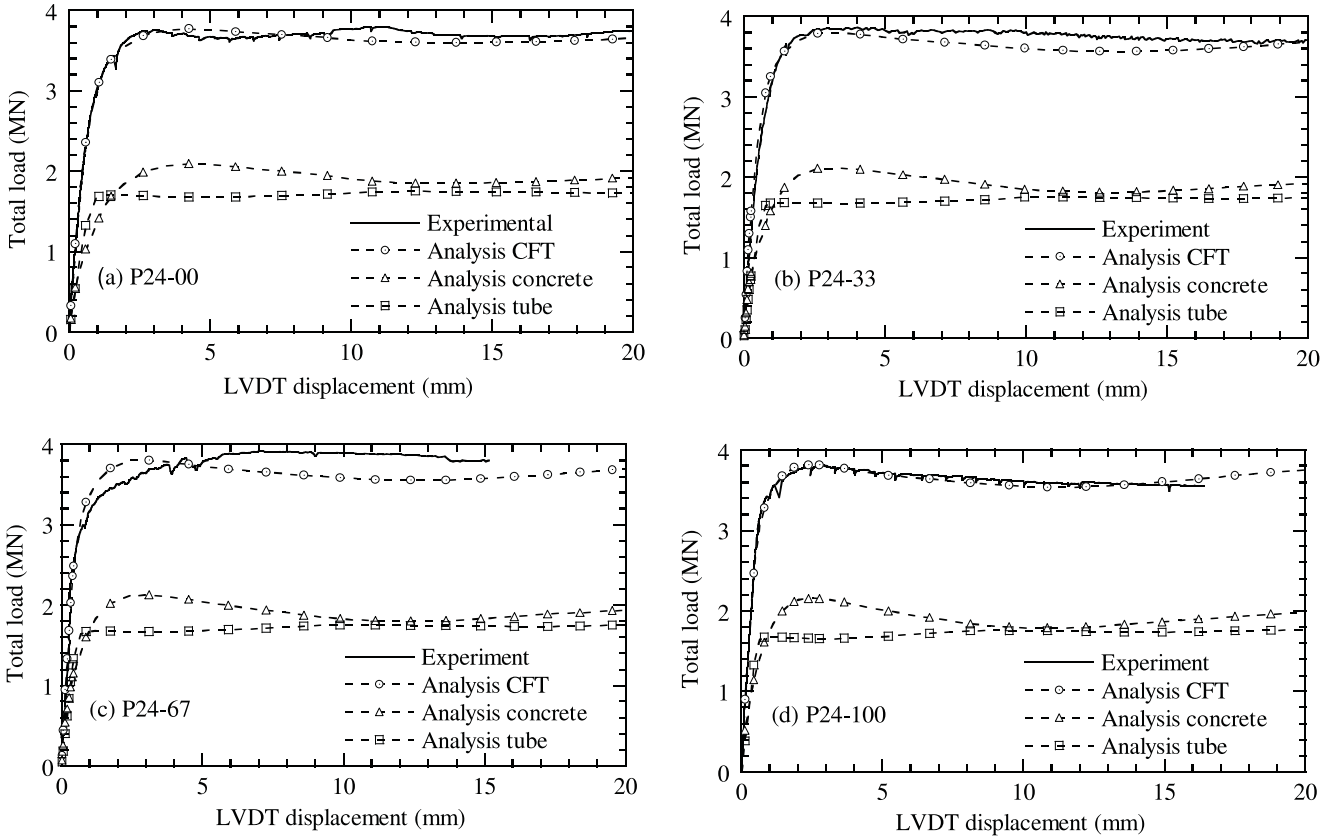

Fig. 17. Load–displacement curves of specimens P24-00, P24-33, P24-67 and P24-100.

analyses, $k_3 = 0.6$ is used for CFT column without gusset plate and $k_3 = 0.45$ is used for CFT columns with gusset plate.

4.2. Simulations of the strength factor k_4

The strength factor k_4 varies between 0 and 1. To make a proper selection of the strength factor k_4, different values of k_4 are used to simulate the behavior of CFT specimens S, P24-00 and P24-100 again. Those selected values of k_4 are $k_4 = 0.5$, 0.75 and 1, respectively. Based on the values of k_3 suggested in the previous section, the load–displacement curves of the experimental data and the numerical results for those specimens are shown in Fig. 10. We can observe that the numerical results with $k_4 = 0.75$ are in good agreement with the experimental data, even though the gusset plates and the loading patterns of these specimens are in quite different arrangements. This justifies the use of $k_4 = 0.75$ in previous section in determining the values of parameter k_3. Similar results are also observed for other CFT columns. Therefore, the value $k_4 = 0.75$ is used throughout the numerical analysis.

4.3. Influence of the friction coefficient

To study the influence of the friction coefficient between the contact surfaces on the behavior of the CFT columns, different values of μ are used to simulate the behavior of CFT specimens P24-00 and P24-100. Those selected values are $\mu = 0$, 0.25, 0.5,

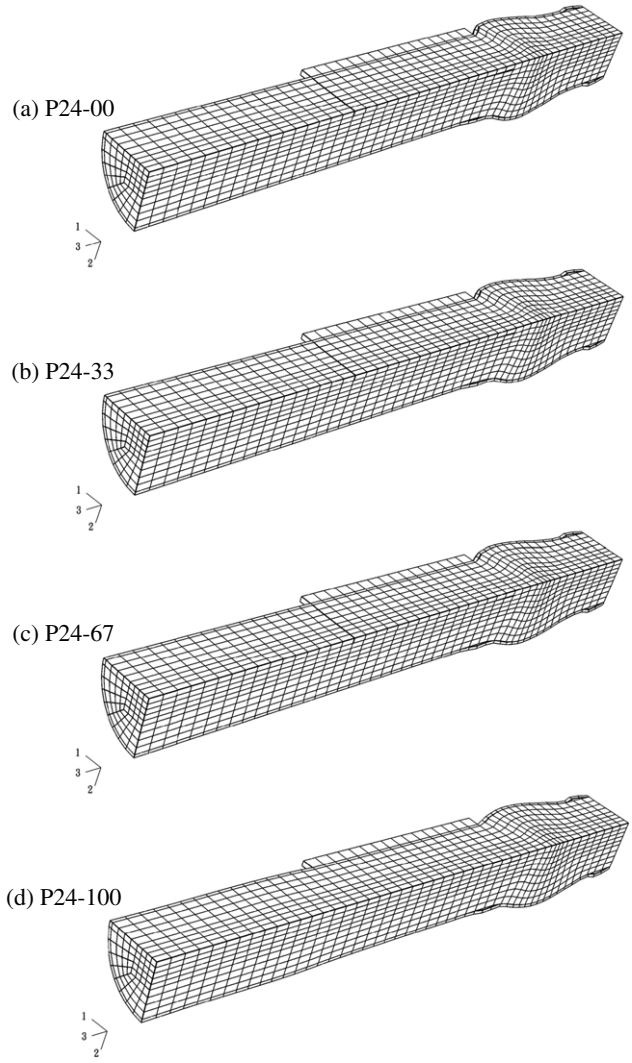

Fig. 18. Deformation shapes of specimens P24-00, P24-33, P24-67 and P24-100.

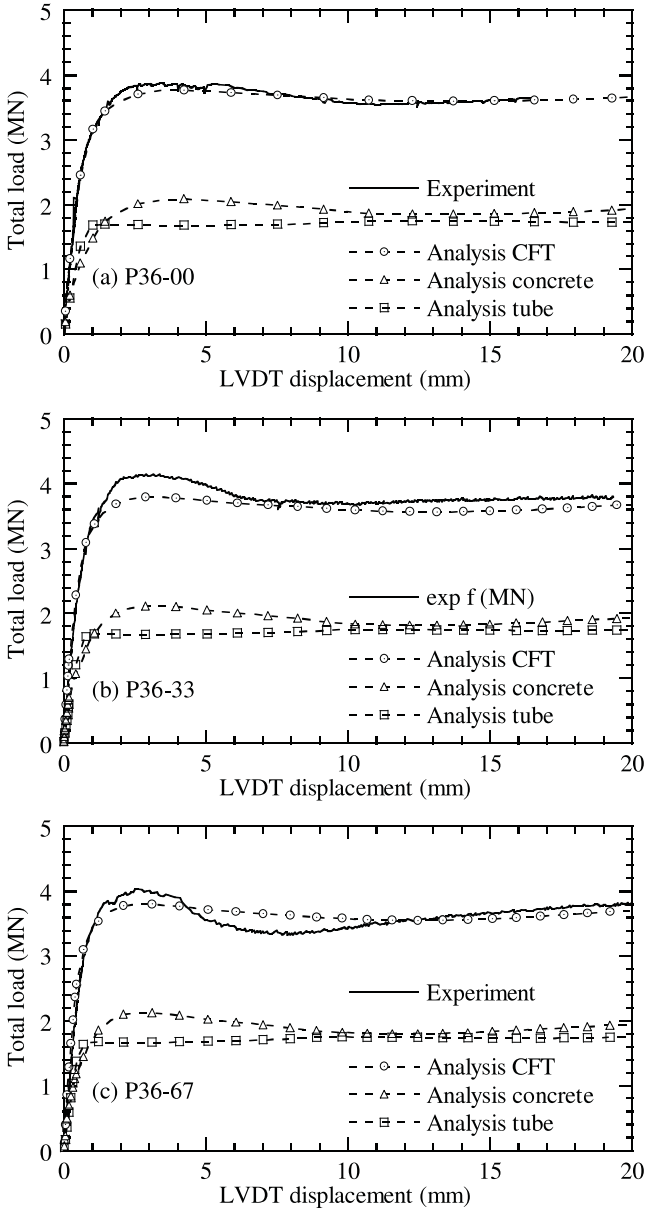

Fig. 19. Load–displacement curves of specimens P36-00, P36-33 and P36-67.

0.75 and 1, respectively. Based on the values of k_3 and k_4 suggested in the previous sections, the load–displacement curves of the experimental data and the numerical results for those specimens are shown in Fig. 11. We can observe that the numerical results with various μ are very close. Similar results are also observed for other CFT columns. This confirms that the value of the friction coefficient μ does not have significant influence on the behavior of the CFT columns.

4.4. Simulations of the S specimen

The S specimen does not have any gusset plate and is subjected to compressive force P_a at the end. The load–displacement curves of the experimental data and the numerical results for S specimen are shown in Fig. 12 and their ultimate loads are listed in Table 2. It can be seen that the result of numerical analysis is very close to the experimental data. In Fig. 12, the reaction forces contributed from concrete and steel tube at the fixed end are also shown. It is clear that the steel tube yields first. After the concrete reaches its ultimate strength, the entire CFT column starts to soften up to failure. Fig. 13 shows the deformation shape of the CFT column as the specimen approaches failure. It can be seen that the concrete core and steel tube still keep in contact to each other and no local bulged shape of the tube takes place.

4.5. Simulations of the P12 specimens

The P12 specimens have gusset plates with 12 mm thickness. The load–displacement curves of the experimental data and the numerical results for P12-00, P12-33 and P12-67 specimens are shown in Fig. 14 and their ultimate loads are listed in Table 2. Generally, the results of the numerical analyses are in good agreement with the experimental data.

The P12-00 specimen is subjected to force P_g applied to the gusset plate only. Probably due to the stress concentration effect around the gusset plate area, part of the concrete core would fail before the yielding of the steel tube occurs (Fig. 14(a)). After the yielding of the steel tube takes place, the concrete can still carry out additional axial load up to its ultimate strength. The P12-33 and P12-67 specimens are subjected to forces P_a and P_g simultaneously. Similarly to the S specimen, the steel tube yields first (Fig. 14(b) and (c)). After the concrete reaches its ultimate strength, the entire CFT column starts to soften up to failure. From Fig. 14 and Table 2 we can observe that the change of the load ratio, i.e. $P_a/(P_a + P_g)$, does not influence the ultimate strength of CFT columns significantly.

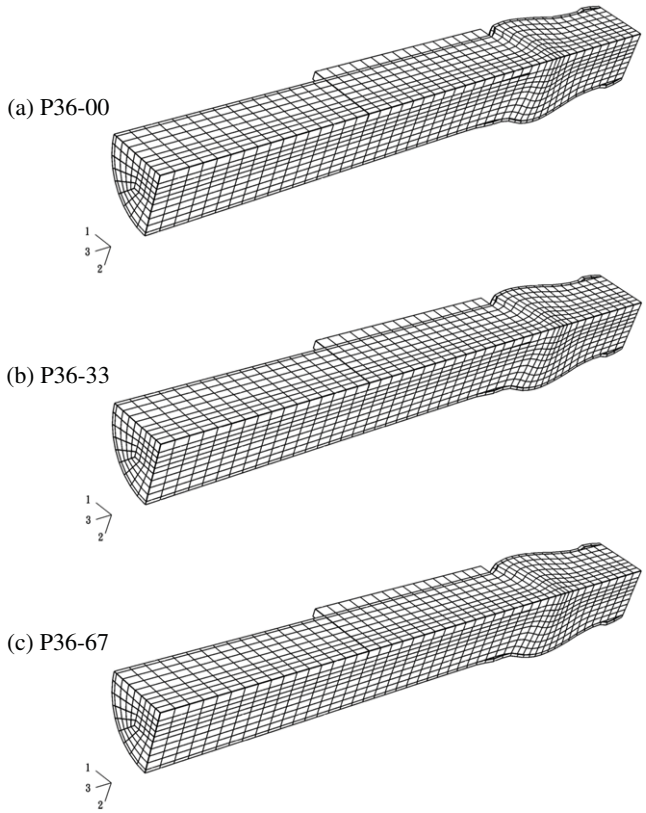

Fig. 20. Deformation shapes of specimens P36-00, P36-33 and P36-67.

Fig. 15 shows the deformation shapes of the CFT columns as the specimens approach failure. It can be seen that the deformation of the column below the gusset plate is greater than those of other places. Bulged shapes of the steel tube take place in the areas close to the gusset plate and the fixed end. This local buckling phenomenon is consistent with the experimental results as shown by the photos [26] in Fig. 16. The local and post-local buckling issues with respect to the circular tubes have been discussed in the work of Bradford et al. [11] and are not duplicated here.

4.6. Simulations of the P24 specimens

The P24 specimens have gusset plates with 24 mm thickness. The load–displacement curves of the experimental data and the numerical results for P24-00, P24-33 P24-67 and P24-100 specimens are shown in Fig. 17 and their ultimate loads are listed in Table 2. Generally, the results of the numerical analyses are in good agreement with the experimental data.

In spite of the loading patterns, the steel tube of all the specimens yields first. After the concrete reaches its ultimate strength, the entire CFT column starts to soften up to failure. From Fig. 17 and Table 2 we can observe again that the change of the load ratio does not influence the ultimate strength of CFT columns significantly. However, when the load ratio becomes large, the CFT column would exhibit more softening behavior after its ultimate strength been reached. In addition, we might conclude that the ultimate strengths of the CFT columns slightly increase with the increasing of the load ratio.

Fig. 18 shows the deformation shapes of the CFT columns as the specimens approach failure. Again, it can be seen that the deformation of the column below the gusset plate is greater than those of other places. Local bulged shapes of the steel tube might take place in the areas close to the gusset plate and the fixed end. Comparing Fig. 18 with Fig. 15, we can conclude that the increasing of the thickness of the gusset plate does not influence the failure patterns of CFT columns significantly.

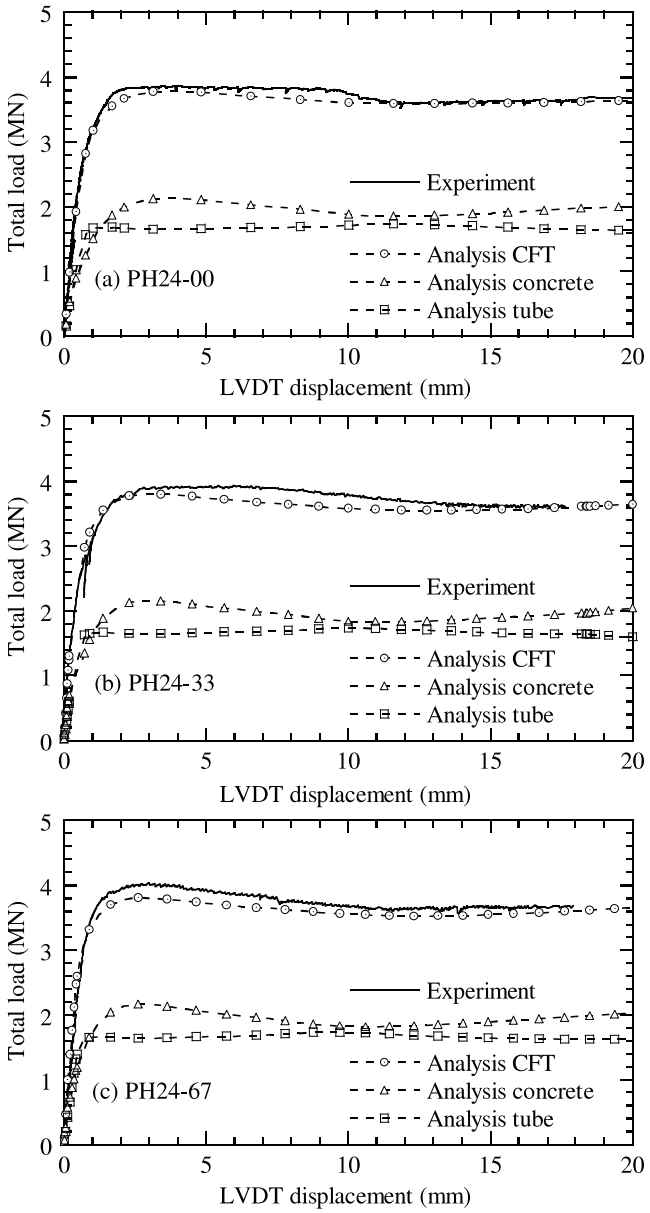

Fig. 21. Load–displacement curves of specimens PH24-00, PH24-33 and PH24-67.

4.7. Simulations of the P36 specimens

The P36 specimens have gusset plates with 36 mm thickness. The load–displacement curves of the experimental data and the numerical results for P36-00, P36-33 and P36-67 specimens are shown in Fig. 19 and their ultimate loads are listed in Table 2. Generally, the results of the numerical analyses are in good agreement with the experimental data.

Similar to P24 specimens, the steel tube of all the specimens yields first. After the concrete reaches its ultimate strength, the entire CFT column starts to soften up to failure. Again, the change of the load ratio does not influence the ultimate strength of CFT columns significantly. However, when the load ratio becomes large, the CFT column would exhibit more softening behavior after its ultimate strength been reached. This phenomenon is more prominent for CFT columns having thicker gusset plates than those having thinner gusset plates (Figs. 14, 17 and 19). From Table 2,

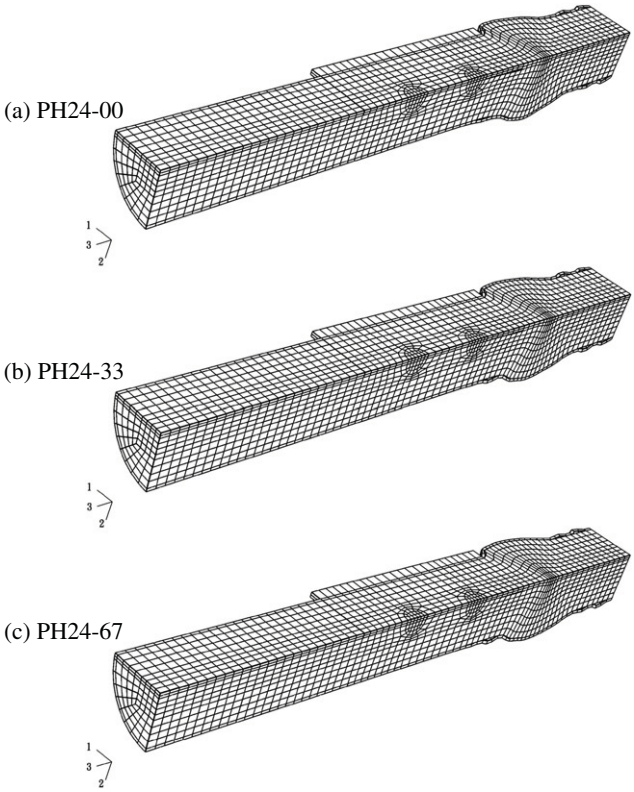

Fig. 22. Deformation shapes of specimens PH24-00, PH24-33 and PH24-67.

we can observe that the increasing of the thickness of the gusset plate does slightly increase the ultimate strength of CFT columns. However, this increasing in the ultimate load is not significantly.

Fig. 20 shows the deformation shapes of the CFT columns as the specimens approach failure. Comparing Fig. 20 with Figs. 18 and 15, we can conclude that the increasing of the thickness of the gusset plate does not influence the failure patterns of CFT columns significantly.

4.8. Simulations of the PH24 specimens

The PH24 specimens have gusset plates with 24 mm thickness and have two circular cutouts on the gusset plates (Fig. 2). The load–displacement curves of the experimental data and the numerical results for PH24-00, PH24-33 and P24-67 specimens are shown in Fig. 21 and their ultimate loads are listed in Table 2. Generally, the results of the numerical analyses are in good agreement with the experimental data.

Similar to the P24 specimens, the steel tube of all the specimens yields first. After the concrete reaches its ultimate strength, the entire CFT column starts to soften up to failure. From Fig. 21 and Table 2, we can observe again that the change of the load ratio does slightly increase the ultimate strength of CFT columns. When the load ratio becomes large, the CFT column would exhibit more softening behavior after its ultimate strength been reached. Comparing the ultimate strengths of PH24 specimens with those of P24 specimens (Table 2), we can see that the introduction of the cutouts on the gusset plates does slightly increase the ultimate strengths of CFT columns. This is because when the concrete fills in the cutouts on the gusset plates, more contact areas are generated between concrete and steel gusset plate. As the result, the entire connection areas are reinforced.

Fig. 22 shows the deformation shapes of the CFT columns as the specimens approach failure. Again, it can be seen that the deformation of the column below the gusset plate is greater than those at other places. Local bulged shapes of the steel tube take place in the areas close to the gusset plate and the fixed end. Comparing Fig. 22 with Fig. 18, we could observe that the introducing of the cutouts on the gusset plate causes more local bulged shapes on the steel tubes below the connection area. This is also consistent with the experimental results as shown by the photos [26] in Fig. 23.

4.9. Simulations of the PH36 specimens

The PH36 specimens have gusset plates with 36 mm thickness and have three circular cutouts on the gusset plates (Fig. 2). The load–displacement curves of the experimental data and the numerical results for PH36-00, PH36-33 and P36-67 specimens are shown in Fig. 24 and their ultimate loads are listed in Table 2. Generally, the results of the numerical analyses are in good agreement with the experimental data.

Similar to the P36 specimens, the steel tube of all the specimens yields first. After the concrete reaches its ultimate strength, the entire CFT column starts to soften up to failure. From Fig. 24 and Table 2, we can observe again that the change of the load ratio does slightly increase the ultimate strength of CFT columns.

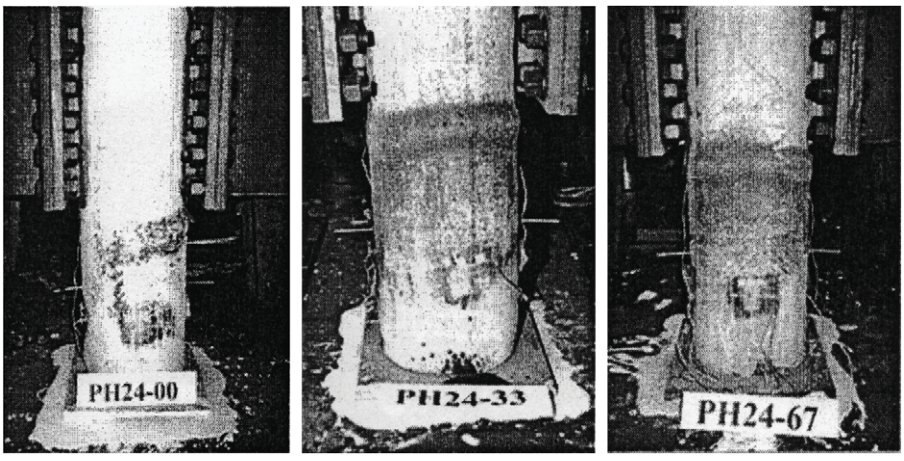

Fig. 23. Failure patterns of specimens PH24-00, PH24-33 and PH24-67 [26].

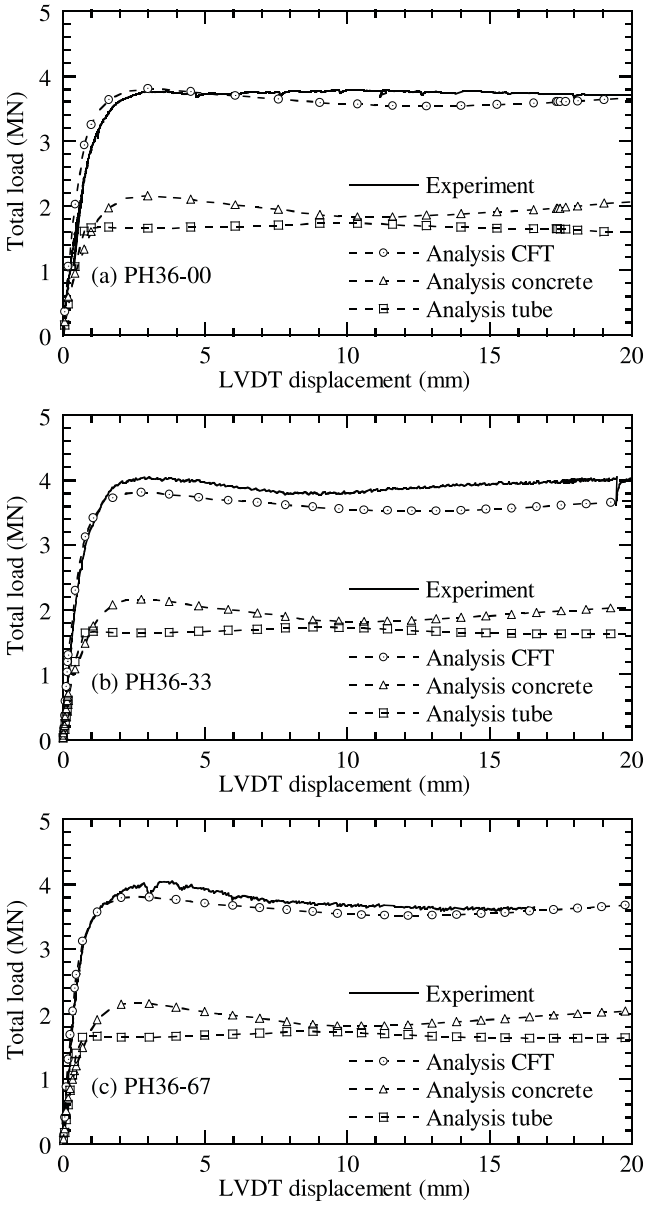

Fig. 24. Load–displacement curves of specimens PH36-00, PH36-33 and PH36-67.

When the load ratio becomes large, the CFT column would exhibit more softening behavior after its ultimate strength been reached. Comparing the numerically calculated ultimate strengths of PH36 specimens with those of P36 specimens (Table 2), we can see that the introduction of the cutouts on the gusset plates does slightly increase the ultimate strengths of CFT columns. However, this phenomenon is not observed in the experimental data and more investigation is needed.

Fig. 25 shows the deformation shapes of the CFT columns as the specimens approach failure. Again, it can be seen that the deformation of the column below the gusset plate is greater than those at other places. Local bulged shapes of the steel tube take place in the areas close to the gusset plate and the fixed end. Comparing Fig. 25 with Fig. 20, we could also observe that the introducing of the cutouts on the gusset plate causes more local bulged shapes on the steel tubes below the connection area.

5. Conclusions

In this paper, nonlinear finite element analyses of CFT-to-Bracing connections subjected to axial compressive force

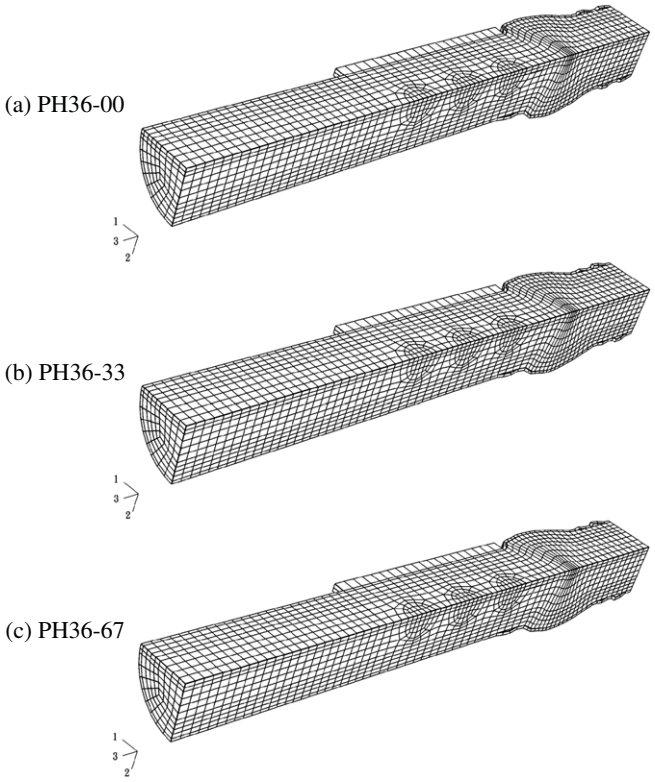

Fig. 25. Deformation shapes of specimens PH36-00, PH36-33 and PH36-67.

are performed. Based on the numerical results, the following conclusions may be drawn:

(1) The value of the friction coefficient μ between the concrete–tube contact surface, the concrete–gusset plate contact surface and the tube–gusset plate contact surface does not have significant influence on the behavior of the CFT-to-Bracing connections.
(2) When the load ratio becomes large, the CFT column with gusset plate would exhibit more softening behavior after its ultimate strength been reached. This phenomenon is more prominent for CFT columns having thicker gusset plates than those having thinner gusset plates. In addition, the ultimate strengths of the CFT columns might slightly increase with the increasing of the load ratio.
(3) The deformation of the CFT column below the gusset plate is greater than those of other places. Local bulged shapes of the steel tube might take place in the areas close to the gusset plate and the fixed end.
(4) The increasing of the thickness of the gusset plate and the introduction of the cutouts on the gusset plates slightly increase the ultimate strengths of CFT columns. Generally, the use of thicker gussets or holes in the gussets is to increase the force transfer of the gusset connection. The holes and thicker gusset should increase the connection transfer capability but they would not affect the column capacity too much.
(5) The introducing of the cutouts on the gusset plate would cause more local bulged shapes on the steel tubes below the connection area under the failure stage.

Acknowledgements

This research work was financially supported by the National Science Council, Republic of China under Grant NSC 92-2625-Z-006-004.

References

[1] Furlong RW. Strength of steel-encased concrete beam–columns. J Struct Div, ASCE 1967;93(ST5):113–24.
[2] Knowles RB, Park R. Strength of concrete filled steel tubular columns. J Struct Div, ASCE 1969;95(ST12):2565–87.
[3] Ge HB, Usami T. Strength of concrete-filled thin-walled steel box columns: experiment. J Struct Eng, ASCE 1992;118(1):3036–54.
[4] Boyd FP, Cofer WF, McLean D. Seismic performance of steel-encased concrete column under flexural loading. ACI Struct J 1995;92(3):355–65.
[5] Bradford MA. Design strength of slender concrete-filled rectangular steel tubes. ACI Struct J 1996;93(2):229–35.
[6] Shams M, Saadeghvaziri MA. State of the art of concrete-filled steel tubular columns. ACI Struct J 1997;94(5):558–71.
[7] Schneider SP. Axial loaded concrete-filled steel tubes. J Struct Eng, ASCE 1998; 124(10):1125–38.
[8] Roeder CW, Cameron B, Brown CB. Composite action in concrete filled tubes. J Struct Eng, ASCE 1999;125(5):477–84.
[9] Uy B. Strength of concrete filled steel box columns incorporating local buckling. J Struct Eng, ASCE 2000;126(3):341–52.
[10] Elchalakani M, Zhao XL, Grzebieta RH. Concrete-filled circular steel tube subjected to pure bending. J Construct Steel Res 2001;57(11):1141–68.
[11] Bradford MA, Loh HY, Uy B. Slenderness limits for filled circular steel tubes. J Construct Steel Res 2002;58(2):243–52.
[12] Elremaily A, Azizinamini A. Behavior and strength of circular concrete-filled tube columns. J Construct Steel Res 2002;58(12):1567–91.
[13] Huang C-S, Yeh Y-K, Liu G-Y, Hu H-T, Tsai KC, Weng YT, et al. Axial load behavior of stiffened concrete-filled steel columns. J Struct Eng, ASCE 2002; 128(9):1222–30.
[14] Hu H-T, Huang CS, Wu M-H, Wu Y-M. Nonlinear analysis of axially loaded CFT columns with confinement effect. J Struct Eng, ASCE 2003;129(10): 1322–1329.
[15] Hu H-T, Huang CS, Chen ZL. Finite element analysis of CFT columns subjected to combined axial force and bending moment. J Construct Steel Res 2005;61(12): 1692–712.
[16] Ellobody E, Young B, Lam D. Behaviour of normal and high strength concrete-filled compact steel tube circular stub columns. J Construct Steel Res 2006; 62(7):706–15.
[17] Lu FW, Li SP, Sun G. A study on the behavior of eccentrically compressed square concrete-filled steel tube columns. J Construct Steel Res 2007;63(7): 941–948.
[18] Schneider SP, Alostaz YM. Experimental behavior of connections to concrete-filled steel tubes. J Construct Steel Res 1998;45(3):321–52.
[19] Elremaily A, Azizinamini A. Design provisions for connections between steel beams and concrete filled tube columns. J Construct Steel Res 2001;57(9): 971–95.
[20] Elremaily E, Azizinamini A. Experimental behavior of steel beam to CFT column connections. J Construct Steel Res 2001;57(10):1099–119.
[21] Johansson M. Composite action in connection regions of concrete-filled steel tube columns. Steel Compos Struct 2003;3(1):47–64.
[22] MacRae G, Roeder CW, Gunderson C, Kimura Y. Brace–beam–column connections for concentrically braced frames with concrete filled tube columns. J Struct Eng, ASCE 2004;130(2):233–43.
[23] Wu LY, Chung LL, Tsai SF, Shen TJ, Huang GL. Seismic behavior of bolted beam-to-column connections for concrete filled steel tube. J Construct Steel Res 2005;61(10):1387–410.
[24] Choi SM, Jung DS, Kim DJ, Kim JH. An evaluation equation of load capacities for CFT square column-to-beam connections with combined diaphragm. Steel and Composite Structures 2007;7(4):287–301.
[25] Abaqus, Inc. Abaqus analysis user's manuals and example problems manuals, version 6.9, Providence (Rhode Island). 2009.
[26] Yang CY. Behavior of CFT-to-bracing connections under axial compression. M.S. thesis. Taipei (Taiwan, R.O.C.): Department of Construction Engineering, National Taiwan University of Science and Technology; 2002 [in Chinese].
[27] ASCE task committee on concrete and masonry structure. State of the art report on finite element analysis of reinforced concrete. New York: ASCE; 1982.
[28] Mander JB, Priestley MJN, Park R. Theoretical stress–strain model for confined concrete. J Struct Eng, ASCE 1988;114(8):1804–23.
[29] Susantha KAS, Ge HB, Usami T. Uniaxial stress–strain relationship of concrete confined by various shaped steel tubes. Eng Struct 2001;23(10):1331–47.
[30] Lam L, Teng JG. Strength models for fiber-reinforced plastic-confined concrete. J Struct Eng, ASCE 2002;128(5):612–23.
[31] Maalej M, Tanwongwal S, Paramasivam P. Modelling of rectangular RC columns strengthened with FRP. Cement & Concrete Composites 2003;25(2): 263–76.
[32] Fam A, Qie FS, Rizkalla S. Concrete-filled steel tubes subjected to axial compression and lateral cyclic loads. J Struct Eng, ASCE 2004;130(4):631–40.
[33] Ellobody E, Young B. Design and behaviour of concrete-filled cold-formed stainless steel tube columns. Eng Struct 2006;28(5):716–28.
[34] Eid R, Paultre P. Plasticity-based model for circular concrete columns confined with fibre-composite sheets. Eng Struct 2007;29(12):3301–11.
[35] Lam L, Teng JG. Stress–strain model for FRP-confined concrete under cyclic axial compression. Eng Struct 2009;31(2):308–21.
[36] Liang QQ, Fragomeni S. Nonlinear analysis of circular concrete-filled steel tubular short columns under eccentric loading. J Construct Steel Res 2010; 66(2):159–69.
[37] Richart FE, Brandtzaeg A, Brown RL. A study of the failure of concrete under combined compressive stresses. Bulletin 185. Champaign (Illinois): University of Illinois Engineering Experimental Station; 1928.
[38] Saenz LP. Discussion of equation for the stress–strain curve of concrete by Desayi P., Krishnan S. ACI J 1964;61:1229–35.
[39] Hu H-T, Schnobrich WC. Constitutive modelling of concrete by using nonassociated plasticity. J Mater Civ Eng, ASCE 1989;1(4):199–216.
[40] ACI committee 318. Building code requirements for structural concrete and commentary (ACI 318-05). Detroit (Michigan): American Concrete Institute; 2005.
[41] Chen C-W. Numerical analysis of CFT-to-bracing connections subjected to axial compressive forces. M.S. thesis. Tainan (Taiwan, R.O.C.): Department of Civil Engineering, National Cheng Kung University; 2003 [in Chinese].